Aperiodic mean-field evolutions in coupled map lattices

Jérôme Losson,[1] Stéphane Vannitsem,[2] and Grégoire Nicolis[1]
[1]*Center for Nonlinear Phenomena and Complex Systems, Université Libre de Bruxelles, Campus Plaine Code Postal 231, 1050 Bruxelles, Belgium*
[2]*Institut Royal Metéorologique de Belgique, Avenue Circulaire 3, 1180 Bruxelles, Belgium*
(Received 18 September 1996; revised manuscript received 19 February 1997)

This paper discusses aperiodic mean-field dynamics in several classes of coupled map lattices (CML's). Two mechanisms underlying complex mean-field evolutions are described. One is the nonlinearity of the mean field evolution equation. The other, at play in locally coupled logistic map lattices, is the presence of ''microscopic'' symmetries. The present work demonstrates that the collective motion in a large class of CML's is governed by a low-dimensional dynamical system which can, in some instances, be obtained explicitly. The paper also reports an interesting kind of mean-field multistability, and discusses the robustness of complex mean-field behaviors under the action of microscopic stochastic perturbations. [S1063-651X(97)04410-3]

PACS number(s): 05.45.+b, 64.60.Cn

I. INTRODUCTION

In this paper we investigate nontrivial collective motion in models framed as coupled map lattices (CML's). We first focus on a globally coupled lattice of piecewise linear maps, and then consider the ubiquitous logistic map lattice. These two systems are representative of two classes of models in which nontrivial collective motion arises for very different reasons. In the piecewise linear map, we show that the origin of complex collective dynamics lies in the remarkable presence of a low-dimensional nonlinear dynamical system which governs the temporal evolution of the mean field. In the logistic maps system, we show that ''microscopic'' symmetries play an important role in the genesis of collective quasiperiodicity. Before reviewing the concept of ''collective motion'' in CML's, we briefly discuss some of the motivations for studying these discrete-time spatially extended models.

In the literature, the appeal of CML's comes from their ability to reproduce experimental situations qualitatively, while remaining amenable to analysis. As experimentalists probe ever deeper into the behavior of systems with a large number of degrees of freedom, new models of globally coupled oscillator arrays are introduced, in which the individual oscillators are either continuous or discrete in time, and whose collective behavior is highly irregular. Some of the experimental situations in which global coupling arises naturally are related to nonlinear optics, with examples ranging from solid-state laser arrays [1] to multimode lasers [2]. In electronics, a number of experiments on Josephson junction arrays coupled in series or in parallel have indicated the presence of very rich dynamics, often related to the multiplicity of attractors, or the linear stability properties of fully synchronized states (cf. Ref. [3], and references therein). The majority of models proposed to describe these dynamics are framed as globally coupled sets of ordinary differential equations (ODE's) [4–6]. The ODE's are usually not rigorously reduced to CML's, and the introduction of the discrete-time map lattices is often motivated by the desire to improve the phenomenological insight into the evolution of the continuous-time oscillators [7]. For example, Wiesenfeld and Hadley [8] found that CML's provided useful reduced systems to investigate the effects of low levels of noise on large globally coupled arrays which possess an even larger number of attractors. In the present paper, we present some insights into the genesis and robustness of highly irregular collective motion in various CML's, with the hope that these might ultimately further our understanding of the nontrivial collective properties of coupled oscillator arrays.

In this context, ''collective'' refers to the properties of global averages, or, more generally, of functions which depend on all the degrees of freedom of the lattice model. The simplest, and most frequently discussed, such quantity is the average activity across a lattice—the mean field. The evolution of these averages is said to be ''nontrivial,'' by convention, if it is nonstationary in the asymptotic temporal regime and in the thermodynamic limit (in which a lattice becomes infinitely large). Furthermore, the hallmark of NTCB is the simultaneous presence of local (or microscopic) chaos. It is worth noting here that the behavior in this limit is investigated directly from an evolution equation for the mean field which is akin to the Perron-Frobenius equation, but which is nonlinear. This approach, explained in detail in Sec. II originally suggested by Kaneko [9] and later used by Pikovsky and Kurths [10] allows us to bypass the problem of finite-size effects.

Three types of NTCB are clearly present in CML's: periodic, quasiperiodic, and chaotic [11,12]. Periodic NTCB can be shown in some prototypical models to reflect a spectral property of the corresponding Perron-Frobenius operator known as asymptotic periodicity (AP). AP is characterized by the cyclical evolution of ensemble densities, and the simultaneous presence of microscopic chaos. No such clear picture has emerged regarding the nature and the origin of collective quasiperiodicity and collective chaos in spite of recent investigations which relate (in partial differential equations) the largest Lyapunov exponent for spatially averaged observables to that associated with the microscopic dynamics [13]. The present work aims at filling this void, for a particular class of CML models.

The major drawback in the analysis of the intrinsic properties of mean-field dynamics is the lack of knowledge of its

equation of motion. Therefore, the investigation of the nature of the dynamics of these observables should be performed using indirect tools such as the computation of correlation dimension or Lyapunov exponents from long time records of the mean field. However, these last approaches are only feasible when the observables considered live on a low-dimensional attractor [14]. Since there is no reason to think that the mean field of CML's possess a low-dimensional attractor, we must thus resort to another approach (although, as we demonstrate in this paper, such an attractor sometimes exists). The one adopted here is widely used in atmospheric dynamics to determine the limits of predictability of the atmosphere, and consists of investigating the property of sensitivity to initial conditions of the system through the analysis of the evolution of small initial errors arising from the finite precision of the measuring device [15]. If the system considered is chaotic, the amplitude of the error increases in time until it reaches a size of the order of the size of the attractor, while, if the system is nonchaotic, the amplitude of the error remains small compared to the attractor's size. For a periodic (quasiperiodic) attractor, the error typically oscillates periodically (quasiperiodically), and the amplitude of this oscillation depends on the size of the initial error, and on the various local trajectory velocities on the attractors. Studying the qualitive features of error growth therefore provides an efficient tool to distinguish the chaotic or nonchaotic character of the dynamics.

Section II explores the phenomenology in a toy model which is amenable to some analytic investigations. The collective behavior is then characterized quantitatively in Sec. III, by focusing on the propagation of errors in the mean-field trajectories. In Sec. IV, we reduce the functional equation governing the evolution of the distribution of activity across an infinitely large lattice to a low-dimensional vector transformation. This reduction provides a number of insights into the origin of the collective chaos. The case of quasiperiodic NTCB is discussed in Sec. V. The main results obtained are summarized in Sec. VI.

II. GLOBALLY COUPLED ''TOY'' MODEL

We will focus on a model originally introduced by Pikovsky and Kurths [10] as a simple system which can be ergodic without being mixing. The model turns out to possess very interesting collective properties which range from the traditionally considered stationary and periodic regimes to less understood chaotic ones. It is also remarkable because the evolution equation for the mean field is a low-dimensional vector transformation which can be analytically derived (cf. the Appendix).

The evolution equation of the model is as follows:

$$x_{t+1}^{(i)} = a_\varepsilon(t)(1-|x_t^{(i)}|)-1, \quad i=1,\ldots,N, \tag{1}$$

with

$$a_\varepsilon(t) \equiv a_0 + \frac{\varepsilon}{N}\sum_{j=1}^{N} x_t^{(j)} \tag{2}$$

$$= a_0 + \varepsilon h_t . \tag{3}$$

Throughout this paper, h_t will denote the mean field (or concentration, or spatial average) at time t. We will analyze a few typical cases for which the dynamics of h_t are neither stationary in time nor time periodic.

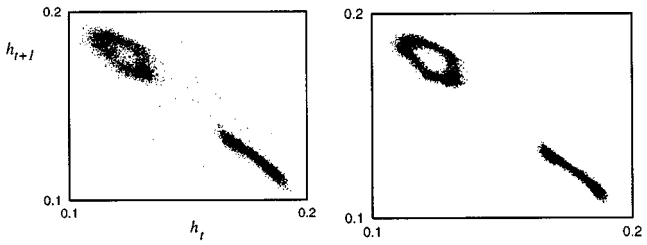

FIG. 1. Left: The return map for the mean field h_t computed on a lattice of 9×10^4 elements, with $a_0=1.9$ and $\varepsilon=-0.74$. Right: The same for a lattice of 10^6 elements, with 10^3 transients discarded.

Figure 1 illustrates a typical nontrivial behavior of the mean field. Here there is no slow convergence to a fixed point or a periodic cycle: the return maps correspond to asymptotic regimes. As reported by Pikovsky and Kurths [10], an important feature is that when the size of the system increases, the fine structure of the attractor is revealed as the finite-size effects gradually disappear. As seen below, these finite-size effects can be very well controlled by focusing directly on a nonlinear version of the Perron-Frobenius equation for the system, thus circumventing the need for brute force simulations of large lattices.

In the limit $N\to\infty$ the mean field can also be computed from the ''collapsed'' density f_t. f_t describes at time t the distribution of activity across an infinitely large network, and it is approximated, when N is finite, by the histogram constructed by binning all the $x_t^{(i)}$'s for fixed t and all i. In other words,

$$\lim_{N\to\infty} h_t = \int_{-1}^{1} u f_t(u)\,du. \tag{4}$$

The probability p that an element of the lattice will have a value between $x-\delta$ and $x+\delta$ is

$$p = \int_{x-\delta}^{x+\delta} f_t(u)\,du. \tag{5}$$

Clearly $\int_{-1}^{1} f_t(u)\,du = 1$. Let

$$S_t(x) \equiv (a_0+\varepsilon h_t)(1-|x|)-1, \quad h_t \equiv \int_{-1}^{1} y f_t(y)\,dy. \tag{6}$$

In essence, Eq. (6) is just a tent map with a time-dependent slope, and the associated Perron-Frobenius operator is similar to the expression for the standard tent map (cf. Ref. [16])

$$f_{t+1}(x) \equiv \mathcal{P}_{S_t} f_t(x) = \frac{1}{a_\varepsilon(t)}\left[f_t\!\left(\frac{x}{a_\varepsilon(t)}\right)\chi_{[-1,0]}(x) + f_t\!\left(1-\frac{x}{a_\varepsilon(t)}\right)\chi_{[0,1]}(x)\right] \tag{7}$$

(with, as usual, $\chi_{[a,b]}(x)=1$ if $x\in[a,b]$, and 0 otherwise). Though Eq. (7) looks deceptively simple, it is nonlinear be-

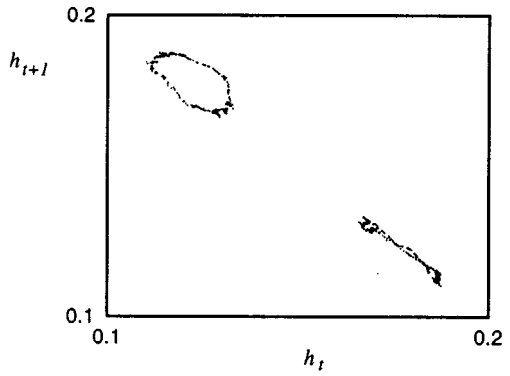

FIG. 2. Return map for the mean field computed from direct numerical integration of Eq. (7), for the same parameters as those of Fig. 1.

cause of the slope's dependence on the density f_t, and it can generate very irregular trajectories for the densities f_t (and thus the mean field h_t).

The return map of Fig. 2, obtained by the numerical solution of Eq. (7), clearly confirms the tendency shown in Fig. 1. It is indeed indicative of a fine-structure attractor which persists in the thermodynamic limit. The accuracy of the algorithm used to generate Fig. 2 is approximately 10^{-4}. As discussed in Sec. IV, it is possible to do much better, but this entails a more geometrical description of the action of Eq. (7) on densities. Before proceeding to this geometrically based description, it is instructive to clarify exactly which kind of mean field evolutions are displayed by system (1).

III. CHARACTERIZATION OF THE MEAN-FIELD DYNAMICS

The investigation of the dynamical properties of averaged observables is hampered by our lack of knowledge of their equations of motion [17]. This implies the need for using algorithms developed in the context of time series analysis (i.e., computation of the correlation dimension, Lyapunov exponents [18]). But these tools become practically inapplicable when the dimension of the attractor becomes large [18]. These limitations prompt the introduction of an alternative method to classify the mean-field dynamics in systems such as Eq. (1) since there is *a priori* no reason to believe that the evolution of mean fields in such models will be governed by very few degrees of freedom. This alternative method is based on the qualitative features of error growth in mean-field trajectories at various parameter values.

Let $\mathbf{x}_0 \in \mathbb{R}^N$ denote the initial state of a transformation of $\mathbb{R}^N$, and $\mathbf{x}_0' = \mathbf{x}_0 + \boldsymbol{\epsilon}_0$ denote a perturbed state displaced from the reference $\mathbf{x}_0$ by a small error $\boldsymbol{\epsilon}_0$. The instantaneous error between the two trajectories $\mathbf{x}_t$ and $\mathbf{x}_t'$ evolving from these initial conditions will be

$$E_t \equiv |\mathbf{x}_t - \mathbf{x}_t'|, \tag{8}$$

where $||$ is a suitably defined vector norm. In the limits of infinitely long time and infinitely small initial error, Eq. (8) grows exponentially with a rate equal to the largest Lyapunov exponent in the system, a quantity independent of the initial condition. But in practice, these double limits can never be achieved and as a result local variability is unavoidable. It is therefore necessary to adopt a probabilistic perspective in order to obtain properties which are independent of the initial condition $\mathbf{x}_0$ [19]. The mean error is then defined to be

$$\langle E_t \rangle \equiv \int_{\mathbb{A}} f_*(\mathbf{x}_0) |\mathbf{x}_t - \mathbf{x}_t'| d\mathbf{x}_0, \tag{9}$$

where f_* is the invariant probability density of occupation of the attractor $\mathbb{A}$. An additional averaging over $\boldsymbol{\epsilon}_0$ can be performed if necessary. The temporal evolution of $\langle E_t \rangle$ provides interesting insights into the properties of the system generating the trajectory $\{\mathbf{x}_t\}$.

In chaotic dynamical systems, the temporal evolution of Eq. (9) follows a ''universal'' pattern: During a short initial period, the error remains small and its evolution is well described by a linearized set of equations [19]. This is followed by a second regime, during which the error increases linearly in time because of nonlinear effects which are no longer negligible. Finally, in the asymptotic regime, the error saturates, and fluctuates around the mean distance separating two arbitrarily chosen points on the attractor. When the behavior is periodic or quasiperiodic, the mean error tends to oscillate (periodically or quasiperiodically), and it typically remains smaller than the average distance separating two randomly chosen points on the attractor (unless very special sets of initial conditions are chosen). These qualitative differences therefore provide efficient means of distinguishing between the various forms of collective behavior, and we now proceed to an investigation of mean error dynamics in the Pikovsky-Kurths model.

As a first numerical experiment, a small random perturbation uniformly supported on $[-5\times10^{-11}, 5\times10^{-11}]$ is added to each $x_{t_*}^{(i)}$ of transformation (1), at an arbitrarily chosen, but large, time t_*. This in turn induces a small initial error in the mean field of the model. Figure 3 displays the mean error growth curves associated to the mean fields for the various coupling strengths. The norm used here to compute Eq. (8) is the two-dimensional Euclidean norm because we work numerically with a plane projection of the mean-field attractor. The attractor dimension will in general depend on the parameter values, and, for complicated regimes, there is no reason to expect that this dimension will be two. But for $\varepsilon = -0.74$, for example, it seems that the attractor is essentially composed of two closed curves, and that the distances separating points on this curve should meaningfully be computed with the two-dimensional Euclidean norm. Given our lack of information for the attractor dimension in other regions of parameter space, the same norm is used when the attractors are more complex.

Clearly, the mean error curves presented in Fig. 3 for $\varepsilon = -0.1$, -0.74, and -1 with 2×10^6 elements display a similar initial exponential behavior which ends when the mean error attains a value of the order of 5×10^{-4}. After this first regime, explained below, two different types of error evolution appear: for $\varepsilon = -0.1$ the error saturates immediately and oscillates around a level which is close to the initial error; for $\varepsilon = -1$ and for $\varepsilon = -0.74$, the the mean error in-

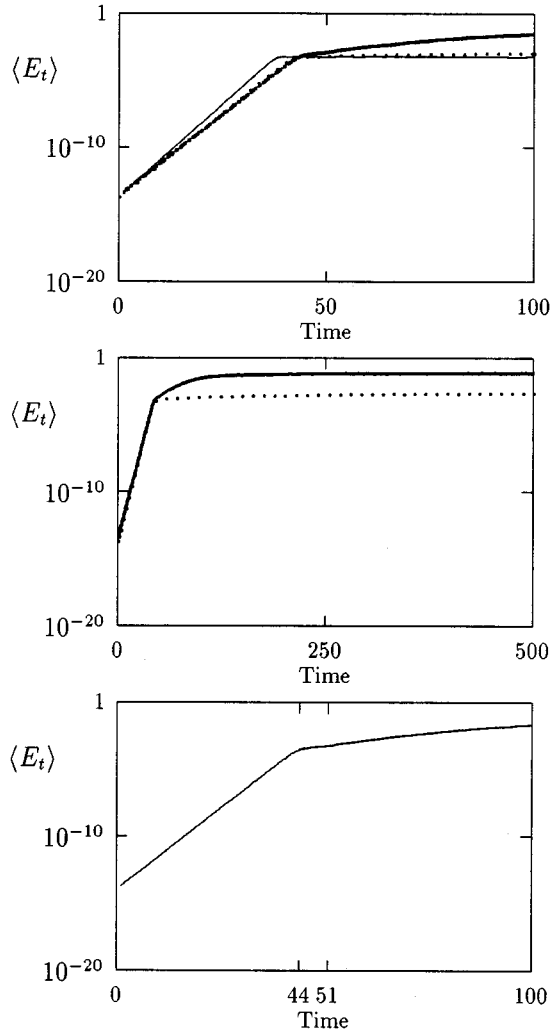

FIG. 3. Growth of an initial perturbation in the CML model (1) with $a_0=1.9$ and $N=2\times10^6$. Top: Superposition of the error growth when $\varepsilon=-0.1$ (thin solid line), -0.74 (dotted line), -1 (thick line). The initial exponential regime is due to the microscopic chaos. For $\varepsilon=-0.1$, the attractor is a mean field. For $\varepsilon=-0.74$ and -1, the attractor is more complicated (cf. Fig. 7). Middle: $\varepsilon=-0.74$ and -1 traces viewed on a different scale to illustrate the long time error growth following the initial exponential regime. Bottom: Error growth $\varepsilon=-1$ and $N=10^7$. Note the second exponential regime between steps 44 and 51.

creases with a growth rate smaller (0.1 time unit^{-1} in the case $\varepsilon=-1$) than the one corresponding to the first exponential regime (0.55 time unit^{-1}). At very large times, the error finally saturates.

To understand the origin of the first exponential behavior for the three parameters of Fig. 3, we follow Pikovsky and Kurths and write the mean field in this finite-size system as a sum of two contributions

$$h_t=\overline{x_t}+\frac{D_t}{N^{1/2}}\,\xi_t, \tag{10}$$

where $\overline{x_t}=\int x f_t(x)dx$; $D_t=\int(x-\overline{x_t})^2 f_t(x)dx$ and ξ_t are Gaussian random variables. In this picture, the origin of the fluctuations ξ_t is the microscopic chaos, and so two initially close trajectories, will, at very small scales, diverge from each other exponentially. This generates the initial exponential regime common to all traces of Fig. 3. As one would expect from Eq. (1), the slope of the initial segments decreases as ε decreases. In addition, its value (0.55 time units^{-1} for $\varepsilon=-1$) corresponds to an estimate of the largest Lyapunov exponent which is consistent with Eq. (1) when $a_0=1.9$, $\varepsilon=-1$, $h_t\simeq0.1$.

Note that the numerical results presented in the figure confirm the validity of Eq. (10): the saturation of the initial exponential regime takes place at scales which are of order $1/\sqrt{N}$. In the limit that $N\to\infty$, displayed in Fig. 4, discussed below, this regime disappears altogether.

After the initial growth of errors due to the microscopic dynamics, the mean-field behaviors for $\varepsilon=-0.74$ and $\varepsilon=-1$ appear to be different from one another. There is no clear exponential behavior for the former while a short exponential regime appears for the latter which reflects the chaotic character of the mean-field dynamics at a macroscopic scale (10^{-3} and above). This confirms the existence of ''collective chaos'' [10,20]. This is a very interesting phenomenon which suggests that, in some spatially extended models, large scale observables might display a higher predictability than small-scale ones (while retaining some of the complexity characteristic of the microscopic dynamics). This change in predictability resulting from changing the scale of averaging should receive further attention in the future.

Finally, note that for both $\varepsilon=-0.74$ and -1, the long-term behavior of the error is a slow increase which eventually stops when the error is comparable to the ''attractor size'' (data not shown in the figure). This slow increase is not observed for the periodic mean-field regime, when $\varepsilon=-0.1$.

It is desirable to investigate mean-field dynamics in the thermodynamic limit $N\to\infty$, a limit which can be simulated by integrating Eq. (7) directly with standard routines (a much finer approach is also developed later in Sec. IV). In this context, however, our perturbing methodology must adapt to the fact that we are no longer dealing with a CML whose components can be perturbed individually. Instead, computations are performed directly on a time series of the mean field h_t obtained from the nonlinear Perron-Frobenius equation (7).

A natural way to address the problem might have been to perturb the density itself, thus indirectly perturbing the mean field, to then follow the simultaneous evolutions of the perturbed and unperturbed time series, and to repeat the process in order to take averages. The problem with this approach is that it assumes that the perturbed and unperturbed solutions will eventually settle on the same attractor. This is not a reasonable hypothesis here; in fact, we will see in Sec. IV that the Pikovsky-Kurths system can possess different coexisting attractors.

In order to circumvent the problem, we adopt a technique developed and used in the field of atmospheric dynamics since the beginning of the century [21]. This method consists in finding in a long historical record atmospheric patterns which resemble one another, and was devoted in its early applications to classification purposes and long range forecasts [22]. This technique is known as the method of analogs. Lorenz [23] used it to estimate the predictability of the

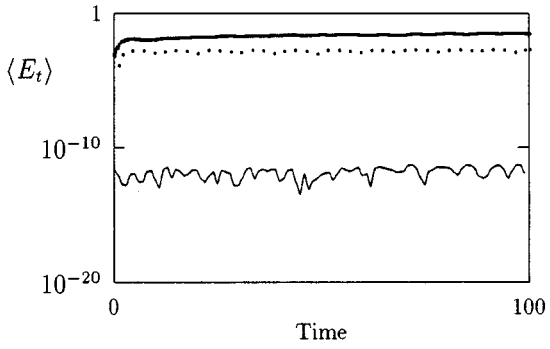

FIG. 4. Illustration of the error growth by direct simulation of the nonlinear Perron-Frobenius equation (7). Same parameters as for Fig. 3. From top to bottom the lines display error propagation traces for $\varepsilon=-1$, -0.74, and -0.1. The main difference with Fig. 3 is the absence of the initial exponential regime due to the microscopic fluctuations. This figure was produced with the method of analogs described in the text, using 300 analogs.

atmosphere directly from experimental data rather than from inherently imperfect models. The approach consists of the following steps.

(1) Consider a very long time series of the desired measurement [the mean field for system (1) in our case].

(2) Set aside a segment of the original time series from $t=t_*$ (a large arbitrarily chosen time) to $t=t_*+\mathcal{N}$ as a reference to be used in step 3 ($\mathcal{N}$ is a parameter in the method; we chose $\mathcal{N}=2$ for reasons discussed below).

(3) Scan the time series for $t>t_*+\mathcal{N}$ until a segment of length $\mathcal{N}$ which is ''close'' to the reference segment previously stored is found (closeness obviously depends on the definition of a suitable norm to measure the differences between time-series segments; we pick the Euclidean norm in $\mathbb{R}^{\mathcal{N}}$).

(4) The reference segment chosen at step (2) and the one found at step (3) form a ''pair of analogs.'' Let t_*^{an} denote the starting time of the analog segment.

(5) Compute the differences $D(i)\equiv|x_{t_*+\mathcal{N}+i}-x_{t_*^{\mathrm{an}}+\mathcal{N}+i}|$ for $i=1,\ldots,L$ (L is another parameter of the method. We chose generally $L=100$ or $L=1000$).

(6) Repeat steps (2)–(5) and average the differences $D(i)$.

The differences between pairs of analogs are thought of as ''small'' initial errors whose evolutions are analyzed in analogy to what is done in Eq. (8). Here, explicit equations of motion are not required, and there is no need to perturb the phase-space trajectories in order to study the subsequent evolution of these perturbations.

Figure 4 shows the mean error evolution, averaged over about 300 pairs of analogs, of the mean field obtained by direct integration of the Perron-Frobenius equation for the two parameter values $\varepsilon=-0.74$ and -1. The analogs were chosen by selecting close mean fields for the data displayed in Fig. 2. Despite the small number of realizations, a clear trend for the mean error evolution emerges, indicating a sensitivity to initial conditions. But the shape of the curves differs markedly from the one displayed in Fig. 3: the initial exponential regime is absent. This absence reflects that the limit $N\to\infty$ is taken in Eq. (10). But there is another mechanism possibly responsible for the elimination of the second

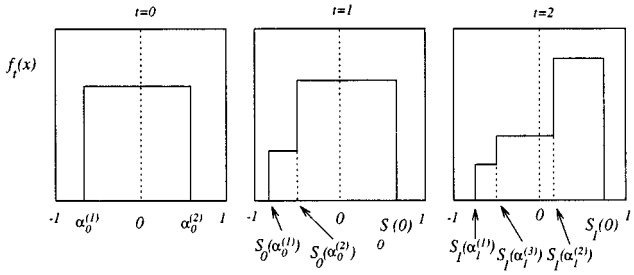

FIG. 5. Two successive densities f_t (solid line) and f_{t+1} (dashed line) in the asymptotic regime (10^6 transients were discarded). Parameters are $a_0=1.9$ and $\varepsilon=-0.74$. This figure was obtained from direct numerical integration of Eq. (7).

exponential error growth regime (when $\varepsilon=-1$). The analogs used to produce Fig. 4 are chosen from a two-dimensional plane projection of the mean-field attractor. Because this projection distorts the latter, two analogs might not actually correspond to two states which are close on the attractor. In this case the linear theory of the evolution of small perturbations does not hold, and there is no reason to expect initial exponential error growth.

The results of Figs. 3 and 4 show clearly that that there is sensitivity to initial conditions at the level of mean-field dynamics for $\varepsilon=-0.74$ and -1, even in the thermodynamic limit. Hence, in light of these results, the initial description of the attractor for $\varepsilon=-0.74$ and that of the sequence of bifurcations described in Ref. [10] for $a=1.9$ and decreasing ε must be revisited. But this is a numerically intensive task which cannot be undertaken by direct integration of the nonlinear Perron-Frobenius equation. Instead, we make use of the piecewise linear nature of transformation (1) to reduce in Sec. IV the nonlinear Perron-Frobenius equation to a vector transformation which, as it will turn out, is acting on a surprisingly low-dimensional space.

IV. DERIVING A LOW-DIMENSIONAL ''MEAN FIELD MAP''

The cornerstone of this approach is the (numerical) observation that the solutions of equation (7) are piecewise constant. Furthermore, the number of ''plateaus'' or piecewise constant segments which are needed to represent the density with a prescribed accuracy increases very slowly with the inverse of the resolution. The relation between the accuracy of the approximation and the number of plateaus depends on the parameters of the model and is briefly discussed at the end of this section (cf. Fig. 5 below). Recently, Morita used these observations to construct a matrix approximation to the operator governing the evolution of collapsed densities in globally coupled tent map lattices [12]. The approach described below generalizes his description to any CML satisfying the following conditions.

(1) The microscopic transformation is the same for all sites.

(2) It is piecewise linear.

(3) Each site is coupled to all others, and the coupling is spatially isotropic.

When the three assumptions above are met, then a vector approximation to Eq. (7) can be derived by using essentially geometrical arguments.

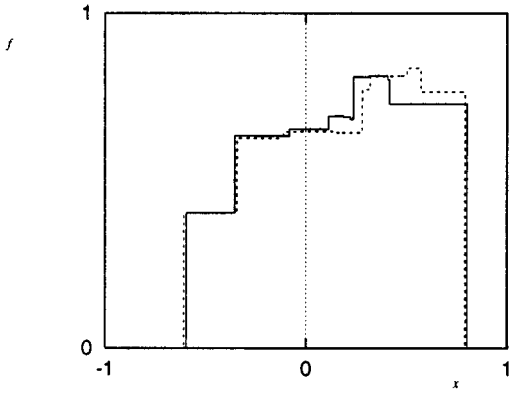

FIG. 6. Schematic illustration of the evolution of an initially constant density. Typically, one plateau is created with each iteration, but at the same time the amplitude of each existing discontinuity decreases by a factor $a_\varepsilon(t)$. As a result, the number of ''significantly'' different plateaus does not diverge in time (cf. Fig. 5).

A. Iteration of a constant density

Suppose $f_0(x)\equiv c_0$ for all $x\in[\alpha_0^{(1)},\alpha_0^{(2)}]$, where $-1<\alpha_0^{(1)}<0<\alpha_0^{(2)}<1$. We now calculate $f_1(x)=\mathcal{P}_{S_0}f_0(x)$. Let $\alpha_1^{(1)}\equiv S_0(\min(|\alpha_0^{(1)}|,|\alpha_0^{(2)}|))$, $\alpha_1^{(2)}\equiv S_0(\max(|\alpha_0^{(1)}|,|\alpha_0^{(2)}|))$, and $\alpha_1^{(\max)}\equiv S_0(0)$. Then Eq. (7) yields

$$f_1(x)=\begin{cases}\dfrac{c_0}{a_\varepsilon(t)} & \forall x\in[\alpha_1^{(1)},\alpha_1^{(2)}]\\[2ex] \dfrac{2c_0}{\alpha_\varepsilon(t)} & \forall x\in[\alpha_1^{(2)},\alpha_1^{(\max)}].\end{cases}\tag{11}$$

Figure 5 displays an initially constant density and its first and second iterates. The simplicity of this example allows us to highlight some key features of this iteration process which hold when f_0 is a more complicated function.

(i) If the support of a density f_t includes the origin, then f_{t+1} is ''folded'' because the iterate of $x=0$ is always the upper bound for the support of f_{t+1}.

(ii) If $|\alpha_0^{(i)}|\neq|\alpha_0^{(j)}|\forall i\neq j$, this folding implies the creation of a discontinuity [at $\alpha_1^{(2)}=S_0(\alpha_0^{(2)})$ in Fig. 5]. This is the only possible mechanism via which the number of piecewise constant segments of the density can increase. With these observations in mind, it is straightforward to consider the evolution of more general initial densities.

B. Iteration of a piecewise constant density

Let $\mathcal{I}$ denote a set of densities such that if $f_t\in\mathcal{I}$, it can be written

$$f_t(x)=\sum_{i=1}^{N} c_t^{(i)}\chi_{I_t^{(i)}}(x),\quad \text{with } I_t^{(i)}\equiv[\alpha_t^{(i)},\alpha_t^{(i+1)})\subset[-1,1]\tag{12}$$

[$\chi_I(x)=1$ if $x\in I$, $\chi_I(x)=0$ otherwise], with the ordering

$$-1<\alpha_t^{(1)}<\alpha_t^{(2)}<\cdots<\alpha_t^{(l-1)}<0<\alpha_t^{(l+1)}<\cdots<\alpha_t^{(N+1)}<1.$$

Here $l=l(t)$ is always chosen such that $\alpha_t^{(l)}=0$. A density $f_t\in\mathcal{I}$ can be described completely by the $(2N+1)$-dimensional vector

$$\mathbf{f}_t:\{\alpha_t^{(1)},\ldots,\alpha_t^{(N+1)},c_t^{(1)},\ldots,c_t^{(N)}\}.\tag{13}$$

If all iterates of f_t belong to $\mathcal{I}$, the Perron-Frobenius operator can be considered as a $2N+1$-dimensional vector transformation. Typically however, if $f_t(x)\in\mathcal{I}$, then $f_{t+1}(x)\notin\mathcal{I}$ unless $f_t(x)$ contains as a discontinuity the preimage of $x=0$ [i.e., there is $\alpha_t^{(i)}$ such that $S_t(\alpha_t^{(i)})=0$]. To remedy this problem, we *impose* $\alpha_{t+1}^{(l)}\equiv 0$, and relabel the $c_{t+1}^{(i)}$'s and $\alpha_{t+1}^{(i)}$'s accordingly even if there is no ''real'' discontinuity in the density at $x=0$. The addition of $\alpha_{t+1}^{(l)}=0$ to $\mathbf{f}_{t+1}$ results in an increase of the vector's dimension. To keep the dimension of $\mathbf{f}_{t+1}$ equal to that of $\mathbf{f}_t$ for all times, one α_{t+1} (and the corresponding c_{t+1}) must then be removed.

To this end, note that S_t decreases the amplitude of existing discontinuities by a factor of $a_\varepsilon(t)$ at every iteration, and so at time T some of the discontinuities are of amplitude $O(\langle a_\varepsilon\rangle_t^{-T})$ where $\langle\ \rangle_t$ denotes time averaging. For example, with $a_0=1.9$, $\varepsilon=-0.74$, numerically it is seen that $\langle a_\varepsilon\rangle_t\sim 1.75$, so the amplitude of the smallest discontinuities at time $T=50$ should be of order 10^{-12} (for an initially flat density), an estimate which turns out to be consistent with direct numerical simulations.

Now suppose that a *strictly constant* $f_0(x)$ (so all c_0's are equal) is approximated by a vector as in Eq. (13) with, say, $N=50$. There are enough components (i.e., 101) in the vectors $\mathbf{f}_0$, $\mathbf{f}_1,\ldots,\mathbf{f}_{50}$ to approximate with any accuracy the evolution of the densities f_0, $f_1,\ldots,f_{50}$. For $t>50$, the density possesses more than 50 discontinuities, so theoretically, the 101-dimensional vector description of the density ceases to hold. But by the argument given in the preceding paragraph, some of the discontinuities $\Delta_t^{(i)}=|c_t^{(i)}-c_t^{(i-1)}|$ will be smaller than $\delta=10^{-12}$ for $t>50$. (In the rest of this paper, δ will be referred to as the *tolerance* of our approximation, and is not to be confused with the overall *accuracy* of the approximation.) By neglecting one of these small-amplitude discontinuities at every iteration, while adding the discontinuity arising from the image of $x=0$, the dimension of the approximating vector $\mathbf{f}_t$ is kept constant. Of course, to obtain an exact expression for the vector approximation to Eq. (7), some bookkeeping is required (indices are changed because of the addition and subtraction of discontinuities), but the conceptual foundations require no additional ingredient. The algorithm is described in detail in the Appendix and illustrated in Fig. 6. Figure 7 displays various return maps obtained for several parameter values.

C. Closeness of the vector approximation to the functional equation

From Sec. IV B, it is clear that if the initial density is represented with a vector as in Eq. (13) with $N=50$, the resulting error in the average h_t induced by this approximation can at most be of order 10^{-12}, and this in turn translates into a similar error on the slope $a_\varepsilon(t)$. So we are naturally led to the question of how closely the vector system stays to the original continuous one [i.e., Eq. (7)]. This issue is re-

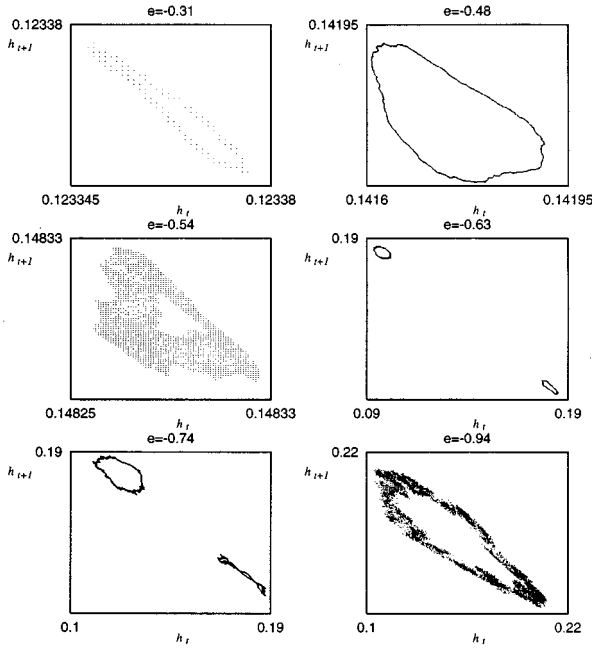

FIG. 7. Return maps h_{t+1} vs h_t for $a_0=1.9$ and various values of the coupling parameter ε. The only periodic cases here are observed for $\varepsilon=-0.31$ and -0.54; in all other panels, the evolution of h_t is either quasiperiodic or chaotic, with initial errors either oscillating around a fixed level, or increasing exponentially. All panels were obtained with $N=50$ equal cells. The tolerance δ defined in Sec. IV B is 10^{-11}.

lated to the ''shadowing'' of Eq. (7) by Eq. (13), and it is rather distinct from that discussed in Sec. IV B, which is the sensitivity to initial conditions in either Eqs. (7) or (13). Note that both issues are themselves not to be confused with the dependence on initial conditions displayed at the level of single trajectories for the CML. The problem discussed here is the behavior of density trajectories, not that of individual (or CML) trajectories.

Given that the effect of approximating the functional equation by a vector transformation is a perturbation in the slope $a_\varepsilon(t)$ (resulting from a perturbation in the average h_t as explained at the end of the Appendix), the issue of how closely the evolution of the discrete system will lie to that of the original one is related to the structural stability of the (density) trajectories of Eq. (7). Although we have not analytically investigated the structural stability of the attractor for the functional equation, we rely on our numerical experiments to postulate this stability in some regions of the (a_0,ε) plane: the attractors for h_t are the same (within the numerical error), whether the CML is integrated directly, Eq. (7) is solved with standard routines, or Eq. (13) is iterated with the algorithm described in the Appendix. Since Eq. (13) is by orders of magnitude the fastest way to go about simulating the dynamics of h_t, we will describe the behavior of h_t using this vector approximation.

D. Effects of noise vs truncation errors

If the tolerance δ is large enough it is possible to induce spurious bifurcations which are similar to the ones arising when white noise in injected in Eq. (7) by including a stochastic component to the slope $a_\varepsilon(t)$, and using instead of the deterministic value, the expression

$$\tilde{a}_\varepsilon(t)\equiv a_0+\varepsilon h_t\xi, \tag{14}$$

where ξ is a random variable uniformly distributed on some subinterval of $[-1,1]$. Figure 8 displays the similarity between the effects of including noise in the system, and those resulting from an inappropriate truncation of the number of plateaus.

This simple numerical experiment indicates how one should study the (spurious) effects which a faulty approximation of the original functional equation can have on the numerical simulations: These effects will be akin to noise-induced transitions. But studying such phenomena is not the purpose of the present paper. We will always choose the approximation with a tolerance small enough to guarantee that we do not induce undesired bifurcations. This is done by picking the combination of δ and the number of cells in the approximation to be such that a reduction of the former and an increase in the latter does not have discernable effects on the collective dynamics.

E. Characterization of the collective attractors

One of the motivations for introducing the vector approximation to the nonlinear Perron-Frobenious equation is that it is very efficient. We were thus able to investigate extensively the ''collective bifurcation diagram.'' The results of these numerical studies are summarized below, and presented in Figs. 8 and 9.

(1) The presence of collective quasiperiodicity in model (1) is not confirmed. A closer look at what appears to be quasiperiodic motion in Eq. (7) (when $a_0=1.9$ and $\varepsilon=-0.74$, for instance) reveals that there are still error propagation (illustrated already in Figs. 3 and 4). This is not what is observed in quasiperiodic systems (cf. Sec. V). Further numerical work is needed to characterize the transition from statistical stability to statistical chaos in system (1).

(2) We identify a type of multistability: the ''collective attractor'' depends on the initial density for the Perron-Frobenius equation. This multistability is remarkable because it is more than a change in the amplitude of an otherwise qualitatively unchanging attractor reported in Ref. [20] in globally coupled tent maps. Such amplitude changes are also observed in systems displaying periodic NTCB, and they are a consequence of the spectral properties of the Perron-Frobenius operator [24]. Figure 9 displays a rather different phenomenon: the qualitative features of the attractor can change drastically if the initial density in Eq. (7) crosses the boundaries of various basins of attraction.

In addition to giving rapid access to some fascinating phenomenology, the vector approximation presented in Sec. IV B highlights the fact that there is a large reduction in the numbers of degrees of freedom which are responsible for the bulk of the collective motion. This is not unlike the situation of certain partial differential equations whose dynamics can be shown to essentially belong to a low-dimensional submanifold of the original infinite-dimensional phase space.

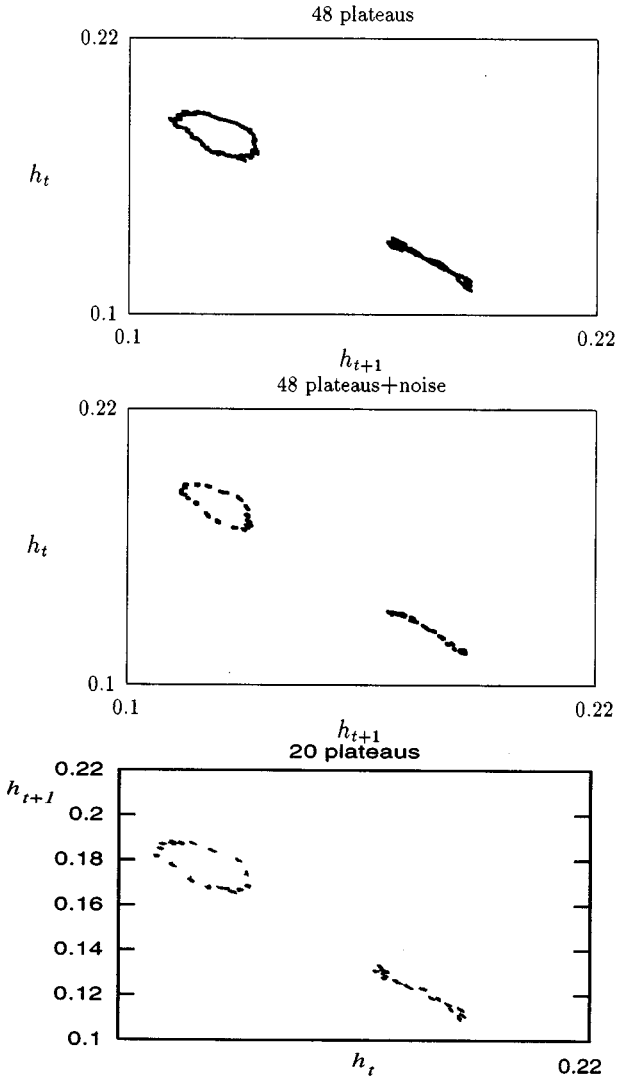

FIG. 8. Top: Return map for $a_0=1.9$ and $\varepsilon=-0.74$, with $N=48$ in Eq. (13), and $\delta=10^{-12}$. Middle: Return map for the mean field obtained from the same 48-cell approximation applied to the stochastic model (7) with the slope given by Eq. (14), with noise uniformly supported on $[-1.5\times10^{-3},1.5\times10^{-3}]$. Bottom: The return map obtained in the deterministic equation (7), with a 20-cell approximation of the density, with $\delta=3\times10^{-3}$.

F. Discussion

The nonlinear transfer operator (7) can be represented by a low-dimensional vector transformation because the densities f_t can be written as a linear combination of basis functions (12). This, in turn, reflects the properties of the space of functions left invariant by the nonlinear operator (7): these spaces must be compact.

The fact that the basis functions in Eq. (12) are piecewise constant facilitates the algebra, but it is not essential. What is essential, is the possibility to represent the densities in a relatively low-dimensional basis. Recently, Alonso *et al.* showed that such bases exist for single logistic maps in large regions of parameter space [25]. Furthermore, the numerics of Kaneko [26] clearly suggest that the distributions of activity for lattices of globally coupled logistic maps can be represented as a low-dimensional linear combination of basis functions. It is therefore probable that the program carried out in Sec. IV can be carried out when the original Pikovsky-Kurths model is replaced by a globally coupled logistic map lattice, and the piecewise constant densities are replaced by the appropriate basis functions. This work lies beyond the scope of the present paper, and we now turn our attention to logistic map lattices which are locally, rather than globally, coupled, because they are representative of a class of systems in which the origin of complex mean field behavior is not a nonlinear transfer operator, but the presence of microscopic symmetries.

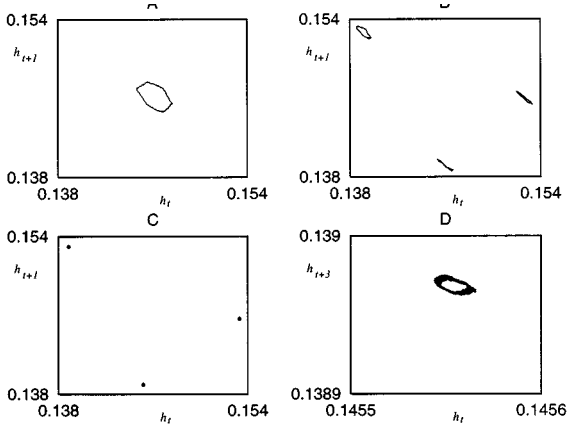

FIG. 9. Illustration of multistability in the mean-field dynamics for model (1). All four return maps were obtained from the vector approximation to Eq. (7), with $a_0=1.9$ and $\varepsilon=-0.52$. (A) The initial density was supported uniformly on $[-0.4,0.494425]$. (B) The initial density was supported uniformly on $[-0.4,0.311108]$. (C) The initial density was supported uniformly on $[-0.35,0.272219]$. (D) Same as in (C), but the scale is changed to display the complex nature of the attractor.

V. COLLECTIVE QUASIPERIODICITY IN LOGISTIC CML's

Collective quasiperiodicity has been reported in hypercubic lattices of democratically and globally coupled logistic maps [11], and in globally coupled tent maps [26,12]. In the latter model, Morita illustrates how the nonlinearity of the operator governing the evolution of collapsed densities can result in quasiperiodic mean-field trajectories.

In this section, we focus on the mean-field behavior of locally coupled logistic maps, because the conclusions of two recent publications [27,28] lead rather naturally to a working hypothesis concerning the origin of collective quasiperiodicity in a class of CML's of which locally coupled logistic maps are representative.

Chaté *et al.* [27] provided strong evidence that collective dynamics in logistic map lattices can be captured by an approximation in which all spatial correlations beyond a certain (small) scale can be neglected. According to these authors, the original CML should then be thought of as a lattice of diffusively coupled ''mesoscopic units,'' each unit being composed of a small number of strongly coupled logistic maps.

In addition, Reick and Mosekilde [28] described conditions under which such units should generate quasiperiodic trajectories: these arise generically in symmetrically coupled systems of identical period-doubling maps. In that case, the

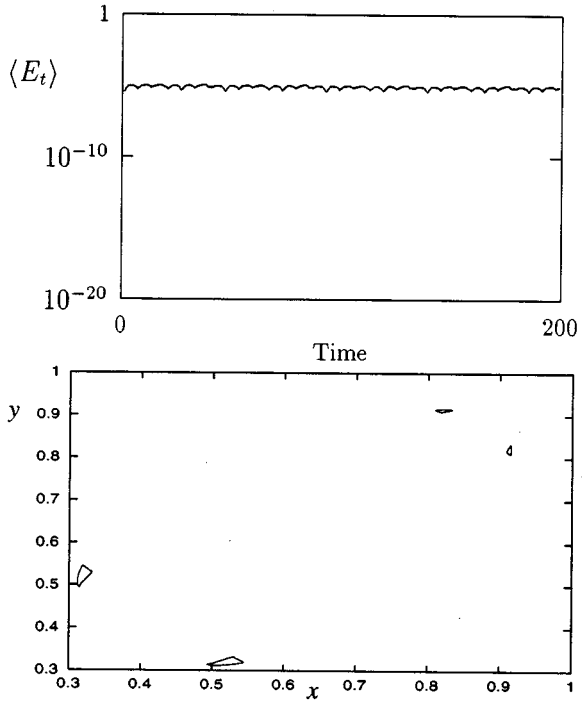

FIG. 10. Top: The temporal evolution of an initial error in the coupled logistic map models (15) and (16) with $r=3.711$ and $\varepsilon=0.1$. Note that, on average, there is no long term increase of an initial error. Bottom: the quasiperiodic attractor for systems (15) and (16) displayed with 10^3 successive iterations.

first two period-doubling bifurcations in the single maps are replaced by two Hopf bifurcations in the coupled system, the second one of which typically generates quasiperiodicity. These quasiperiodic solutions are by nature bistable with the (possibly chaotic) solutions of the single maps, and the basin boundaries separating quasiperiodic and chaotic attractors are extremely complex. Thus ensemble averages for such systems will include contributions from chaotic and from quasiperiodic attractors. For example, consider the two-dimensional transformations

$$T_x(x_t,y_t)\equiv(1-\varepsilon)S(x_t)+\varepsilon S(y_t), \tag{15}$$

$$T_y(x_t,y_t)\equiv(1-\varepsilon)S(y_t)+\varepsilon S(x_t), \tag{16}$$

where $S(x)=rx(1-x)$ and $\varepsilon\in[0,1]$. Figure 10 displays the activity of Eqs. (15) and (16) when it is quasiperiodic, and the propagation of an initial error separating two trajectories. We observe that the error oscillates quasiperiodically, but that it does not slowly increase as in the case ($\varepsilon=-0.74$, $a_0=1.9$) for the Pikovsky-Kurths system (cf. Figs. 3 and 4). Figure 11 displays the return map for an *ensemble* average h_t, when some of the elements in the ensemble evolve quasiperiodically, while others evolve chaotically. Here h_t can be expressed in the asymptotic regime as the sum of two contributions (if there are only two bistable attractors):

$$h_t=\int_{\mathbb{C}} x f_t(x)dx+\int_{\mathbb{Q}} x f_t(x)dx, \tag{17}$$

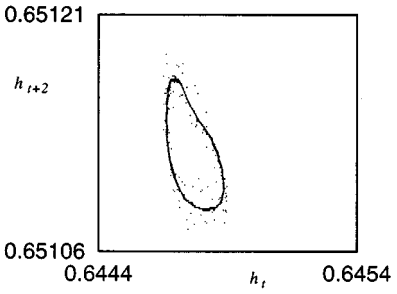

FIG. 11. Return map for the concentration h_{t+2} vs h_t is displayed for an ensemble of 4×10^4 $2D$ logistic maps [Eqs. (15) and (16)] with $\varepsilon=0.15$ and $r=3.711$. The return map h_{t+2} vs h_t is displayed for clarity: h_{t+1} vs h_t possesses two disjoint components which are far apart relative to the size of the one displayed here. The dots which surround the thick line are due to the transients.

where f_t is the probability of occupation of phase space, and $\mathbb{C}$ and $\mathbb{Q}$ denote the chaotic and quasiperiodic attractors, respectively. Numerically, the ensemble is approximated by a finite collection of two-dimensional (2D) maps (which we think of as a lattice of decoupled 2D maps), and the ensemble average is therefore approximated by the mean field for this finite lattice. Here again this mean field can be expressed as the sum of two contributions:

$$h_t=\frac{1}{N}\sum_{j=1}^{N} x_t^{(j)}=\frac{1}{N}\left[\sum_{j\in\mathbb{C}} x_t^{(j)}+\sum_{j\in\mathbb{Q}} x_t^{(j)}\right], \tag{18}$$

where $\mathbb{C}$ and $\mathbb{Q}$ now denote the sets of indices corresponding to sites which evolve chaotically and quasiperiodically, respectively. The $\mathbb{C}$ contribution asymptotically reaches a steady state (plus finite-size fluctuations), while the $\mathbb{Q}$ contribution is responsible for the observed collective quasiperiodicity. The relative importance of the quasiperiodic attractor is reflected in the fact that the finite-size fluctuations associated with the chaotic sites are ''washed out'' when they averaged with the nonfluctuating quasiperiodic components.

This ensemble quasiperiodicity is ''robust:'' It survives when maps (15) and (16) are coupled together diffusively as in the following lattice models [$T_{x/y,t}$ denoting $T_{x/y}(x_t,y_t)$ for short]:

$$x_{t+1}^{(i)}=(1-\eta)T_{x,t}^{(i)}+\frac{\eta}{4}\left[T_{x,t}^{(i+1)}+T_{y,t}^{(i+1)}+T_{x,t}^{(i-1)}+T_{y,t}^{(i-1)}\right], \tag{19}$$

$$y_{t+1}^{(i)}=(1-\eta)T_{y,t}^{(i)}+\frac{\eta}{4}\left[T_{x,t}^{(i+1)}+T_{y,t}^{(i+1)}+T_{x,t}^{(i-1)}+T_{y,t}^{(i-1)}\right], \tag{20}$$

where $\eta\in[0,1]$. Figure 12 displays the collective quasiperiodicity present in the model when $\eta\neq0$ but small. If η is increased further, a complex sequence of collective bifurcations takes place. This sequence depends sensitively on the values of the other parameters ε and r.

In addition to surviving the diffusive coupling of Eqs. (19) and (20), it is interesting to remark that the collective quasiperiodicity is also observed numerically in systems perturbed stochastically. Furthermore, investigating the proper-

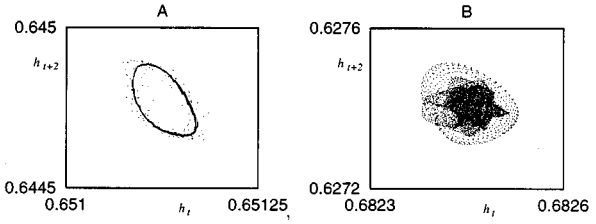

FIG. 12. Return maps h_{t+2} vs h_t for models (19) and (20); same parameters as in Fig. 11, except the ''intercluster'' coupling is now turned on. (A) $\eta=0.001$, and the mean field remains quasiperiodic. (B) Here $\eta=0.09$, and the mean field evolves chaotically. As η is further increased, the mean field undergoes a complex sequence of bifurcations.

ties of stochastic models closely related to Eqs. (19) and (20) is interesting in its own right since it is possible, in stochastic models, to relate theoretically the collective behavior to the spectral properties of the induced transfer operator [24].

Here we describe the phenomenology in models (19) and (20), where Eqs. (15) and (16) are replaced with

$$T^{(i)}_{x,\xi}(x_t,y_t)\equiv(1-\varepsilon)S(x^{(i)}_t)+\varepsilon S(y^{(i)}_t)+\xi^{(i)}_x, \qquad (21)$$

$$T^{(i)}_{y,\xi}(x_t,y_t)\equiv(1-\varepsilon)S(y^{(i)}_t)+\varepsilon S(x^{(i)}_t)+\xi^{(i)}_y, \qquad (22)$$

where the $\xi^{(i)}_{x/y}$ are i.i.d. random variables. Typically, their density $g(\boldsymbol{\xi})$ is supported on a finite (and small) subinterval of [0,1]. If the interval is too large, the noise tends to destroy the apparent quasiperiodic collective behavior, and induces first, periodic evolutions, and eventually, stationary behaviors. Without loss of generality, we take the noise density g to be

$$g(\boldsymbol{\xi})=\prod_{i=1}^{N}\chi_{[l,r]}(\xi^{(i)}_y), \quad 0\leqslant l<r\leqslant 1, \qquad (23)$$

where χ is the usual indicator function. Figure 13 displays a typical return map for Eqs. (19) and (20) with Eqs. (21) and (22) when the noiseless model is quasiperiodic. The figure displays the mean-field return maps both when $\eta=0$, and when $\eta\neq 0$.

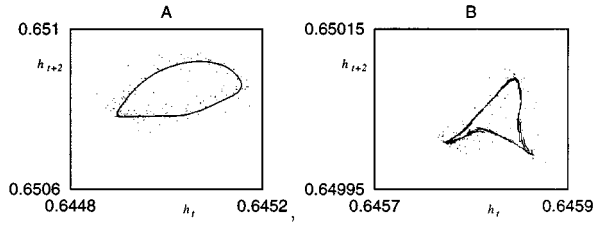

FIG. 13. Return maps for the mean fields of stochastically perturbed lattices of 2D maps [Eqs. (21) and (22)]. As in the previous figures, the map plotted is h_{t+2} vs h_t for clarity. In both cases, the parameters are $r=3.711$, the coupling $\varepsilon=0.15$, and the perturbing noise is uniformly supported on $[-0.00015,0.00015]$. If the noise amplitude is greater than this, the finest scale structures displayed here are destroyed and replaced by ''clouds.'' (A) the 2D maps are uncoupled ($\eta=0$). (B) the 2D maps are coupled ($\eta=0.001$). As in the noiseless case, an increase in η will generate a complex sequence of bifurcations (cf. Fig. 12).

When $\eta=0$, the phase space is the unit square $[0,1]\times[0,1]$. Hence the ensemble density f_t used to determine the mean field h_t,

$$h_t=\int_0^1 y\int_0^1 x f_t(x,y)dx\,dy,$$

evolves under the action of the transfer operator [16]

$$f_{t+1}(x,y)=\int_0^1\int_0^1 f_t(u,v)g(u-T_u(u,v),$$

$$v-T_v(u,v))dv\,du. \qquad (24)$$

Such operators are asymptotically periodic [29], a property which implies that the mean field can only evolve periodically (although the period of the collective cycle can be very high). Hence the return map displayed in Fig. 13(a) is in fact periodic.

When $\eta\neq 0$, the phase space of the CML is now the hypercube $[0,1]^{2N}$, and the transfer operator is the straightforward $2N$-dimensional generalization of (24)

$$f_{t+1}(\mathbf{x})=\int_{[0,1]^{2N}} f_t(\mathbf{u})g(\mathbf{u}-\mathbf{T}(\mathbf{u}))d\mathbf{u}. \qquad (25)$$

Again, these operators are asymptotically periodic, and therefore the *ensemble* averages for the CML's also cycle periodically. But h_t is not an ensemble average for the coupled system. It is an average which reflects the properties of single trajectories.

It is tempting to generalize the conclusion, valid for $\eta=0$, that there is no collective quasiperiodicity when $\eta>0$, and that Fig. 13 in fact displays a periodic cycle with high period. Unfortunately, systems like Eqs. (21) and (22) tend not to be ergodic: the collective attractor, as in the tent maps described in Ref. [20], depends on the initial distribution. Therefore, it is not possible at present to infer from the properties of Eq. (25) those of mean-field trajectories. Despite these theoretical shortcomings, Eqs. (21) and (22) provide some illustration for the robustness of the mean field's attractor, even if a detailed analysis eventually uncovers a loss of true quasiperiodicity, and its replacement by a very high-period limit cycle.

VI. CONCLUSION

The complex mean-field behavior observed in the Pikovsky-Kurths model originates in the nonlinear nature of operator (7), which governs the evolution of the collapsed densities. Remarkably, this operator can be well approximated by a nonlinear vector transformation which is of low dimension (less than 10^2). This reduction of dimension is interesting because it clearly demonstrates that some of the collective properties in large classes of CML's can be investigated with the tools developed to treat low-dimensional dynamical systems.

The essential ingredient for the nonlinearity of the transfer operator is the global coupling, and the essential ingredient for the reduction to a low-dimensional matrix is the existence of a low-dimensional basis which spans the space invariant under the action of the operator. We note that these two

ingredients are present in the globally coupled logistic map lattices discussed in Ref. [20], and that this model should therefore be amenable to analytic investigations (though the algebra will probably be heavier than in the piecewise linear situations described here).

In this framework, we expect that collective motion can display the array of complex behaviors which are characteristic of nonlinear low-dimensional discrete-time transformations. Examples are given by the collective bifurcation diagram (Fig. 7) and by the remarkable coexistence of different chaotic attractors displayed in Fig. 9. Although such transformations can in principle possess quasiperiodic solutions, we note here that we did not find such attractors for model (1), although such attractors were recently reported in a related globally coupled system [12].

Locally coupled logistic map lattices point to an altogether different mechanism responsible for quasiperiodic mean-field evolutions: the presence of quasiperiodic attractors in symmetrically coupled (low dimensional) ''clusters'' of logistic maps results in the quasiperiodic evolution of average in networks of these ''clusters.'' The quasiperiodic attractors are by construction bistable with single map solutions, and when these are chaotic (as in Fig. 11), one generically observes microscopic chaos coexisting in a given lattice with microscopic quasiperiodicity. The working hypothesis linking the collective behavior to that of ''mesoscopic units'' is consistent with the ideas presented in Refs. [27, 28].

In the test model of Sec. V, the collective quasiperiodicity clearly arises from the microscopic quasiperiodicity, and it survives diffusive intercluster coupling. In addition it also survives the addition of small stochastic perturbations. Analysis of the transfer operator in the presence of noise leads to the conclusion that the apparent collective quasiperiodicity is in fact collective periodicity of high period [29].

The present work leaves a number of avenues unexplored. The first is the extension of the present approach to a class of models which are not piecewise constant, but quadratic. Given the ubiquity of transformations possessing quadratic maxima in the modeling literature, it is important to theoretically ground our understanding of collective properties in lattices of coupled logistic maps, and to identify the different mechanisms responsible for nontrivial collective behavior in these models. A related research avenue is to classify the kinds of transitions which separate the various collective regimes. Although in some systems, such transitions have been given preliminary attention [24,20], much remains to be done in this area. For example, although the presence of critical phenomena is undeniable in CML's its relation to the spectral properties of transfer operators is still unclear [24]. Finally, the multistability discussed in Sec. IV E is a remarkable phenomenon, which to our knowledge has not been described previously. It is different in nature from that described in Ref. [20] because the coexisting attractors discussed here are qualitatively different. The structure of the basin boundaries is still unknown, and the basic ingredients which are necessary for the coexistence of multistable collective attractors still need to be identified.

ACKNOWLEDGMENTS

The authors acknowledge fruitful discussions with C. Nicolis. J.L. acknowledges the financial support of the Marie-Curie Fellowship program of the EC's Human Capital and Mobility Program, and receives additional support from the Fonds FCAR (Government of Quebec). This work was supported in part by the Global Change and the Interuniversity Attraction Pole programs of the Belgian Government.

APPENDIX

This Appendix describes in detail the algorithm which is used to simulate the matrix representation of the nonlinear transfer operator (7). It relies heavily on a clear understanding of the geometrical properties of the model (1).

Starting from Eq. (13), the problem is to determine the exact expression for the image vector $\mathbf{f}_{t+1}$ approximating the density f_{t+1} introduced in Sec. IV:

$$\mathbf{f}_{t+1}=\{\alpha_{t+1}^{(1)},\ldots,\alpha_{t+1}^{(N+1)},c_{t+1}^{(1)},\ldots,c_{t+1}^{(N)}\}. \tag{A1}$$

This is done in two steps. The first deals with the α_{t+1}'s, the second with the plateau heights (the c_{t+1}'s). From Eq. (1),

$$\alpha_{t+1}^{(j)}=a_\varepsilon(t)(1-|\alpha_t^{(k)}|)-1, \quad \text{with } j=\Pi_t(k), \tag{A2}$$

where Π_t is some time-dependent permutation of the set $\{1,\ldots,N\}$. To obtain an explicit form for Π_t, note that the closer $|\alpha_t^{(k)}|$ is to $x=0$, the larger its image under Eq. (A2), and hence the larger the index of this image in Eq. (A1). If j is the index of the *image* $\alpha_{t+1}^{(j)}$, then the *preimage* must be such that

$$|\alpha_t^{(j)}|>|\alpha_t^{(j+1)}|, \quad \text{for all } j=1,\ldots,N.$$

Obviously, the α_t's are known, and so the permutation Π_t is easily determined in practice [for example, $\Pi_t(l)=N+1$ for all t]. Computing the c_{t+1}'s is a little trickier.

Note that each constant segment of the initial density f_t, of height $c_t^{(k)}$ on the interval $[\alpha_t^{(k)},\alpha_t^{(k+1)}]$ will be transformed under the action of the transformation S_t into another constant function of height $c_t^{(k)}/a_\varepsilon(t)$ defined on $[\alpha_{t+1}^{\Pi_t(k)},\alpha_{t+1}^{\Pi_t(k+1)}]$. Here the ordering of the original $\alpha_t^{(k)}$'s is not necessarily preserved under the action of the transformation because it is possible to have (with $n>k+1$, $n\in\{1,\ldots,N+1\}$)

$$|\alpha_t^{(k)}|>|\alpha_t^{(n)}|>|\alpha_t^{(k+1)}| \quad \text{and} \quad \alpha_t^{(k)}<\alpha_t^{(k+1)}<0<\alpha_t^{(n)}.$$

Hence the images of the constant segments of f_t can overlap, so that to compute $c_{t+1}^{(j)}$ it is necessary to sum the contributions of all the segments whose images overlap with the interval $[\alpha_{t+1}^{(j)},\alpha_{t+1}^{(j+1)}]$. Define the set $\mathbb{H}_t(j)\subset\{1,\ldots,N+1\}$:

$$\mathbb{H}_t(j):\{1\leqslant k<l \quad \text{such that } [\alpha_{t+1}^{(j)},\alpha_{t+1}^{(j+1)}] \cup[\alpha_{t+1}^{\Pi_t(k)},\alpha_{t+1}^{\Pi_t(k+1)}]\neq\emptyset\},$$

$$\mathbb{H}_t(j)\cdot:\{l\leqslant k\leqslant N+1 \quad \text{such that } [\alpha_{t+1}^{(j)},\alpha_{t+1}^{(j+1)}] \cup[\alpha_{t+1}^{\Pi_t(k+1)},\alpha_{t+1}^{\Pi_t(k)}]\neq\emptyset\}.$$

In other words, the set $\mathbb{H}_t(j)$ contains the indices of the constant segments of f_t whose images overlap with the jth segment of f_{t+1}. With this notation, we have

$$c_{t+1}^{(j)} = \sum_{k \in \mathbb{H}_t(j)} \frac{c_t^{(k)}}{a_\varepsilon(t)}. \tag{A3}$$

Define the integer $2<q<N$ to be such that $\Delta_{t+1}^{(q)} < \overline{\delta}$, while $\Delta_{t+1}^{(i)} > \overline{\delta}$ for $i<q$. To keep the dimension of $\vec{\mathbf{f}}_{t+1}$ equal to that of $\mathbf{f}_t$, $\alpha_{t+1}^{(q)}$ is removed from the vector $\vec{\mathbf{f}}_{t+1}$. Hence $c_{t+1}^{(q-1)}$ and $c_{t+1}^{(q)}$ must be equated, and this is done so that the mass of the interval $[\alpha_{t+1}^{(q-1)}, \alpha_{t+1}^{(q+1)}]$ is unchanged. What is changed here is the value of h_{t+1}, and although the exact perturbation depends on the values of $\alpha_{t+1}^{(q-1)}$, $\alpha_{t+1}^{(q)}$, $\alpha_{t+1}^{(q+1)}$, and $\Delta_{t+1}^{(q)}$, a conservative upper bound on the change in h_{t+1} can easily be seen to be δ itself.

Once the expressions (A2) and (A3) for the vector $\mathbf{f}_t$ are obtained, we carry out the ''approximation'' which consists of (1) eliminating the $\alpha_{t+1}^{(q)}$ corresponding to a small discontinuity, setting $c_{t+1}^{(q-1)}$, $c_{t+1}^{(q)} = c'$ where

$$c' = \frac{c_{t+1}^{(q-1)}(\alpha_{t+1}^{(q)} - \alpha_{t+1}^{(q-1)}) + c_{t+1}^{(q)}(\alpha_{t+1}^{(q+1)} - \alpha_{t+1}^{(q)})}{\alpha_{t+1}^{(q+1)} - \alpha_{t+1}^{(q)}},$$

(2) adding $\alpha_{t+1}^{(l)}$ in the vector $\vec{\mathbf{f}}_{t+1}$, and (3) setting $c_{t+1}^{(l)} = c_{t+1}^{(l-1)}$.

Equations (A1), (A2), and (A3) define the vector transformation which approximates the nonlinear Perron-Frobenius equation, and which can be easily implemented numerically (cf. Fig. 6).

[1] N. Yu, R. K. DeFreez, D. J. Bossert, R. A. Elliott, H. G. Winful, and D. F. Welsh, Electron. Lett. **24**, 1203 (1988).

[2] G. E. James, E. M. Harrell II, and R. Roy, Phys. Rev. A **41**, 2778 (1990).

[3] S. Nichols and K. Wiesenfeld, Phys. Rev. E **49**, 1865 (1994).

[4] P. Hadley and M. R. Beasley, Appl. Phys. Lett. **50**, 621 (1987).

[5] M. Silber, L. Fabiny, and K. Wiesenfeld, J. Opt. Soc. Am. B **10**, 1196 (1993).

[6] J. Swift, S. H. Strogatz, and K. Wiesenfeld, Physica D **55**, 239 (1992).

[7] L. Fabiny and K. Wiesenfeld, Phys. Rev. A **43**, 2640 (1991).

[8] K. Wiesenfeld and P. Hadley, Phys. Rev. Lett. **62**, 1335 (1989).

[9] K. Kaneko, Prog. Theor. Phys. Suppl. **99**, 263 (1989).

[10] A. S. Pikovsky and J. Kurths, Phys. Rev. Lett. **72**, 1644 (1994).

[11] H. Chaté and P. Manneville, Prog. Theor. Phys. **87**, 1 (1992).

[12] S. Morita, Phys. Lett. A **211**, 258 (1996).

[13] S. Vannitsem and C. Nicolis, J. Geophys. Res. **100**, 16 367 (1995).

[14] D. I. Abarbanel, R. Brown, J. J. Sidorowisch, and L. Sh. Tsimring, Rev. Mod. Phys. **65**, 1331 (1993).

[15] S. Vannitsem and C. Nicolis, J. Atmos. Sci. **54**, 347 (1997).

[16] A. Lasota and M. C. Mackey, *Chaos, Fractals and Noise: Stochastic Aspects of Dynamics* (Springer-Verlag, New York, 1994).

[17] C. Nicolis and G. Nicolis, J. Atmos. Sci. **52**, 1903 (1995).

[18] E. Ott, *Chaos in Dynamical Systems* (Cambridge University Press, Cambridge 1993).

[19] C. Nicolis and G. Nicolis, Int. J. Bifurcation Chaos Appl. Sci. Eng. **3**, 1339 (1993).

[20] K. Kaneko, Physica D **86**, 158 (1995).

[21] C. E. P. Brooks and J. Glasspoole, Q. J. R. Meteorol. Soc. **38**, 139 (1922).

[22] R. G. Barry and A. H. Perry, *Synoptic Climatology: Methods and Applications* (Methuen, City, 1973).

[23] E. N. Lorenz, J. Atmos. Sci. **26**, 636 (1969).

[24] H. Chaté and J. Losson, Physica D (to be published).

[25] D. Alonso, D. MacKernan, P. Gaspard, and G. Nicolis, Phys. Rev. E **54**, 2474 (1996).

[26] K. Kaneko, Physica D **55**, 368 (1992).

[27] H. Chaté, A. Lemaître, P. Marcq, and P. Manneville, Physica A **224**, 447 (1996).

[28] C. Reick and E. Mosekilde, Phys. Rev. E **52**, 1418 (1995).

[29] J. Losson and M. C. Mackey, Phys. Rev. E **52**, 1403 (1995).